

Fissile material detection using neutron time-correlations from photofission

R. A. Soltz,^{1,*} A. Danagoulian,^{2,3} E. P. Hartouni,¹ M. S. Johnson,¹
S. A. Sheets,¹ A. Glenn,¹ S. E. Korbly,² and R. J. Ledoux²

¹*Lawrence Livermore National Laboratory, Livermore, CA 94550, USA*

²*Passport Systems Inc., North Billerica, MA 01862, USA*

³*Massachusetts Institute of Technology, Cambridge, MA 02139, USA*

(Dated: February 4, 2019)

The detection of special nuclear materials (SNM) in commercial cargoes is a major objective in the field of nuclear security. In this work we investigate the use of two-neutron time-correlations from photo-fission using the Prompt Neutrons from Photofission (PNPF) detectors in Passport Systems Inc.'s (PSI) Shielded Nuclear Alarm Resolution (SNAR) platform for the purpose of detecting ~ 5 kg quantities of fissionable materials in seconds. The goal of this effort was to extend the secondary scan mode of this system to differentiate fissile materials, such as highly enriched uranium, from fissionable materials, such as low enriched and depleted uranium (LEU and DU). Experiments were performed using a variety of material samples, and data were analyzed using the variance-over-mean technique referred to as Y_{2F} or Feynman- α . Results were compared to computational models to improve our ability to predict system performance for distinguishing fissile materials. Simulations were then combined with empirical formulas to generate receiver operating characteristics (ROC) curves for a variety of shielding scenarios. We show that a 10 second screening with a $200 \mu\text{A}$ 9 MeV X-ray beam is sufficient to differentiate kilogram quantities of HEU from DU in various shielding scenarios in a standard cargo container.

arXiv:1812.03807v2 [physics.ins-det] 1 Feb 2019

* soltz1@llnl.gov

I. INTRODUCTION

Fissile materials refer to materials which, due to their nuclear structure, allow for sustained fission chains. The two most common isotopes which form the basis of fissile materials are ^{235}U and ^{239}Pu . Methods for detecting the presence of fissile materials support the goals of national and international programs for nuclear-nonproliferation. An extensive literature exists on potential identification schemes using active interrogation including neutron probes and delayed and prompt neutron signals [1–5], photon probes and delayed neutron signals [6–12], photon and neutron probes and delayed neutron signals [13–15], and photon probes and fission product radiation [16, 17]. A general review of the various concepts can be found in Ref. [18]. All of these methods use single-particle signals. Multi-particle schemes, usually two- and three-neutron signals have also been pursued, with photon [19, 20] and neutron [21–25] beams as well as in passive interrogation [26–32], where ambient radiations are used to induce the signals. Here we report on an active interrogation method using 9 MeV Bremsstrahlung photons to induce the emission of time-correlated, prompt neutrons measured within the Prompt Neutrons from Photofission (PNPF) system developed at Passport Systems Inc. (PSI) [33–35].

II. TIME-CORRELATION OF FISSION-CHAIN NEUTRONS

A fission chain reaction occurs in fissile material when the neutrons from each fission diffuse through the material and induce subsequent fissions in other nuclei. The neutrons emitted from this process are highly correlated, resulting in neutron count distributions that deviate significantly from Poisson distributions produced by random neutron events.

The theory of fission-chain correlations was initially developed by Richard Feynman while at Los Alamos [36]. The aim of that research was to describe the neutron fluctuations in a reactor pile where the measured neutrons originate from fission chains and random decays. To measure deviations from the Poisson expectation, Feynman defined a normalized second moment,

$$Y_{2F} = \frac{\langle n^2 \rangle - \langle n \rangle^2 - \langle n \rangle}{2\langle n \rangle} \equiv \frac{\text{variance} - \text{mean}}{2 * \text{mean}} \quad (1)$$

where n is the measured neutron count per unit time, and $\langle n \rangle$ and $\langle n^2 \rangle$ represent averages over a series of time-gates. Subtracting the mean from the variance enforces $Y_{2F} = 0$ for the special case of a Poisson distribution, and division by the mean ensures that the quantity is independent of rate. The subscript “2F”, not used in the original paper, has been added by others to credit Feynman and to denote that this quantity is derived from the second moment.

This statistic has been used extensively in the study of nuclear reactor cores [37–41], and it has been extended for time varying sources of the fluctuations, e.g. in accelerator driven cores [42–48]. In these systems the number of neutrons generated spontaneously from radioactive decay greatly exceeds those generated by the introduced beam.

The idea for using the time-correlation for non-destructive inspection of objects containing fissile material has been pursued for “passive” interrogation schemes [21, 22, 24, 26–30, 49–52] (where the natural background initiates the fission chains) and for “active” interrogation schemes [19, 20, 23, 25, 53] (where a beam of particles induces the fission chains).

For neutron-induced fission-chains from an idealized point source, a time-dependent expression for Y_{2F} has been developed by Snyderman and Prasad [54–56],

$$Y_{2F} = \left(1 - \frac{1 - e^{-\lambda T}}{\lambda T}\right) \epsilon \left[1 + \frac{(M - 1)(\nu - 1)}{\nu}\right] \frac{\nu_2}{\nu} (M - 1). \quad (2)$$

where,

- λ = inverse of the neutron correlation time, a convolution of fission-chain and neutron transit times,
- T = time-gate during which neutrons are counted,
- ϵ = neutron detection efficiency,
- M = neutron multiplication, $\frac{1}{1-k}$, where $k = p\nu$ is k-effective and p is the neutron-induced fission probability,
- ν = the first moment, equal to the mean number for the neutron distribution from a single induced fission,
- ν_2 = the second combinatorial moment, half the variance for the neutron distribution from a single fission.

Eq. 2 illustrates utility of Y_{2F} , which increases with the square of the multiplication and is therefore sensitive to the enrichment if the geometry of the object and efficiency of the detector are known. One can construct higher order moments (i.e. $Y_{3F,4F}$) that depend on higher orders of the multiplication, but a corresponding dependence on higher orders of the efficiency makes these statistics more suitable for large acceptance detectors and/or long integration

times due to the reduced coincidence rates. It is also important to note that Eq. 2 is appropriate for neutron beams. In Sec. V we will modify this expression for photon-induced fission-chains in extended objects.

III. EXPERIMENTAL SETUP

To study the feasibility of using photo-induced fissions chains to identify and characterize fissile materials we use a subset of the components of the PSI SNAR platform. The photon beam is generated from electron bremsstrahlung on a water-cooled radiator. The electron current is adjustable and uniform with high duty-cycle. For all experiments a 9 MeV electron kinetic energy was used. The beam currents are adjustable from 100 to 500 μ Amps. For the results presented here, the beam current was set to 200 μ Amps to avoid the non-Poisson effects of the data acquisition (DAQ) dead time losses. This corresponds to a rate of 2×10^{12} Hz for photons with energies between 2 and 9 MeV, incident on an approximately 10×10 cm square spot size at the target location. The photon beam energy spectrum for the 9 MeV Bremsstrahlung radiator is shown in Fig. 1.

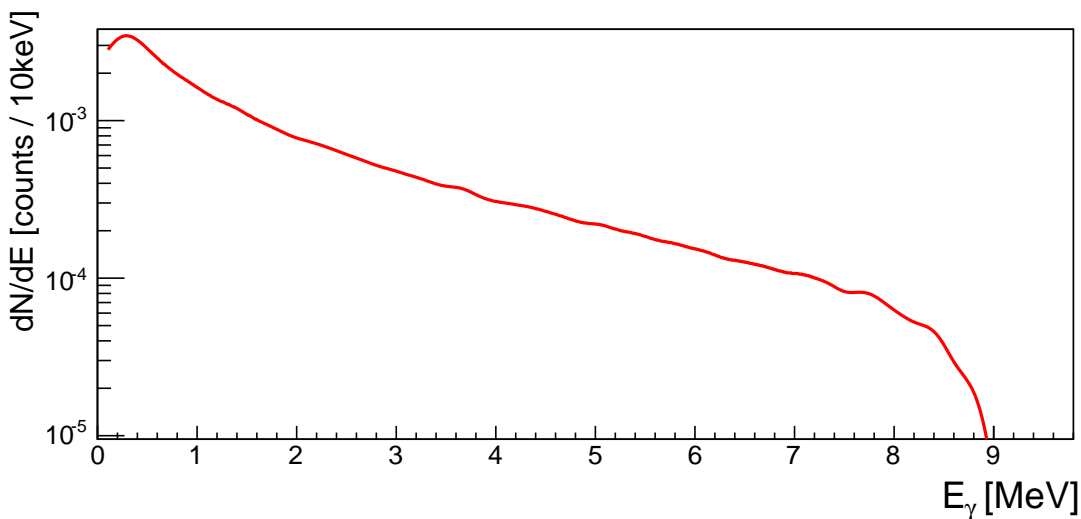


FIG. 1. Photon energy spectrum in PSI's SNAR system, calculated with a GEANT4 simulation.

The full SNAR configuration is shown in Fig. 2. The PNP detectors consist of EJ-309 5 inch diameter liquid scintillator detectors coupled to 5" Hamamatsu photomultiplier tubes arranged in two sets of 2×8 arrays placed on opposite sides of the cargo container. The PNP arrays have ~ 5 cm thick high density polyethylene (HDPE) inserts placed in between the detectors to reduce adjacent detector cross-talk that can lead to an artificial Y_{2F} signal. Before and after tests show that these inserts reduce the cross-talk component by a factor of four.

Measurements of Y_{2F} were made for a set of objects designed to study the relationship between Y_{2F} and neutron multiplication. These objects, listed in Table 1, were constructed from discs of depleted uranium (DU) and highly enriched uranium (HEU), and blocks of low enriched uranium (LEU). The objects were arranged in geometries to achieve a higher range of multiplication values. Fig. 3 shows the stacking arrangement for the three HEU discs. The highest multiplication values were achieved with an interleaved stack of LEU and HEU with HDPE moderators placed above and below the stack to provide neutron reflection. Multiplication values were calculated using MCNP 6.2 [57] run in the kcode mode. The control benchmark was obtained with a beryllium block, in order to generate a large quantity of uncorrelated photo-neutrons anticipated to have no measurable Y_{2F} value. Data were collected from a series of 600-second exposures, which were then combined for each object during the data analysis. Approximately ten exposures were collected for each uranium configuration, with additional exposures taken for the beryllium object.

Material	Dimension	Mass	Mult.	Run Duration
Be block	7.3 x 7.3 x 10.4 cm	0.988 kg	1.000	8360 s
DU 1-disc	0.2 x 5 cm	0.3 kg	1.015	6690 s
DU 2-disc	0.4 x 5 cm	0.6 kg	1.026	6750 s
DU 3-disc	0.6 x 5 cm	0.9 kg	1.035	7080 s
HEU 1-disc	0.2 x 5 cm	0.3 kg	1.061	7080 s
HEU 2-disc	0.4 x 5 cm	0.6 kg	1.109	7080 s
HEU 3-disc	0.6 x 5 cm	0.9 kg	1.155	6960 s
HEU+LEU 1-stack	0.2 x 5 cm 10 x 10 x 2 cm	3.988 kg	1.177	6410 s
HEU+LEU 2-stack	2 (0.2 x 5 cm) 2 (10 x 10 x 2 cm)	7.976 kg	1.304	7240 s
HEU+LEU 3-stack	3 (0.2 x 5 cm) 3 (10 x 10 x 2 cm)	11.964 kg	1.401	6920 s
HEU+LEU 3-stack +HDPE	3 (0.2 x 5 cm) 3 (10 x 10 x 2 cm) 10 x 10 x 1.27 cm	11.964 kg	1.430	7080 s
HEU+LEU 3-stack +HDPE	3 (0.2 x 5 cm) 3 (10 x 10 x 2 cm) 10 x 10 x 2.54 cm	11.964 kg	1.468	6760 s
HEU+LEU 3-stack +HDPE	3 (0.2 x 5 cm) 3 (10 x 10 x 2 cm) 10 x 10 x 3.81 cm	11.964 kg	1.501	5980 s
HEU+LEU 3-stack +HDPE	3 (0.2 x 5 cm) 3 (10 x 10 x 2 cm) 10 x 10 x 5.08 cm	11.964 kg	1.527	7080 s

TABLE 1. List of objects exposed to the 9 MeV Bremsstrahlung beam within the Passport Systems SNAR facility.

IV. DATA ANALYSIS

A. Neutron Identification

The main component of the detection system consists of an array of EJ-309 scintillators, coupled to Hamamatsu photomultiplier tubes (PMT). The choice of the PMTs was based on their < 3 ns rise time, thus retaining the sensitivity to the difference between the two main fast components of the light production from the triplet-triplet annihilation. The increase in triplet-triplet annihilation from the much larger ionization density of the neutron-recoiled proton tracks results in a distinct delay in light output. Neutrons can be distinguished from photons by their relative fractions of fast and slow light output using various Pulse Shape Discrimination (PSD) techniques, and their deposited energies can be quantified. The left panel of Fig. 4 shows a histogram of PSD vs. deposited energy, in electron equivalents, for a set of detector events. The distribution is then split into individual energy bins, and the PSD distribution for every energy bin is fitted with two Gaussians, as can be seen in the right panel of Fig. 4, which shows the 2D cut used to separate neutrons from photons. However, this is not sufficient to suppress the very large photon population, created by the intense $200 \mu\text{A}$ photon beam. Therefore, more sophisticated pulse shape discrimination algorithms were developed to reject the photon pileups, which otherwise would contribute a significant background to the neutron population [35]. Overall, the combined pulse shape analysis allows a suppression of the photon population by a factor of $\times 10^7$, limiting the beam-on background count to only the cosmogenic neutrons.

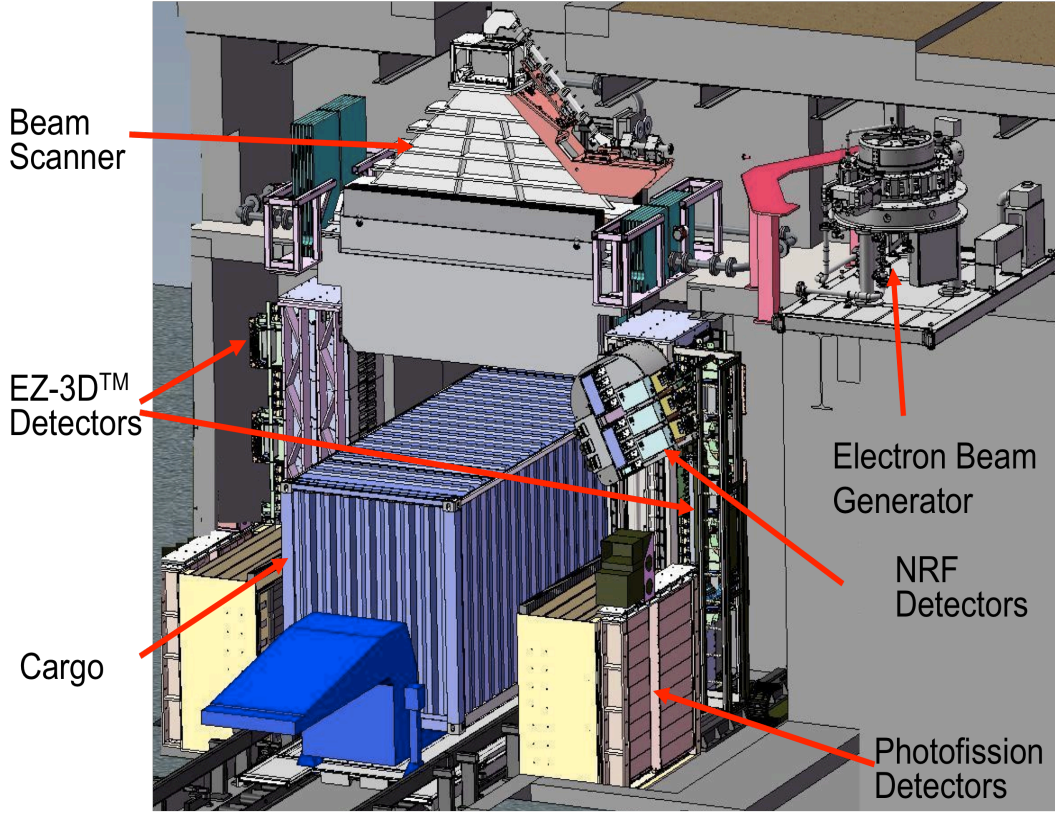


FIG. 2. Configuration for Passport Systems Inc Shielded Nuclear Alarm Resolution (SNAR) platform. This analysis uses the photofission detectors shown on the sides.



FIG. 3. Sample object position for SNAR system data collection.

B. Multiplicity analysis of neutron events

The experimental data were collected in a series of 600-second exposures, with some exposures ending prematurely due to disruptions within the data acquisition system due to the extended run times and need for data synchronization. The identified neutrons in each run were arranged in time-ordered sequence to facilitate binning in time-gates of varying duration. For clarity, we rewrite Eq. 1 above with explicit averages, where sums are taken over sequential time-gates, n refers to the bin-number corresponding to the neutrons detected within a specific time-gate, and b_n is the normalized probability for detecting n neutrons.

$$Y_{2F} = \frac{\sum_n n^2 b_n - (\sum_n n b_n)^2 - \sum_n n b_n}{2 \sum_n n b_n}. \quad (3)$$

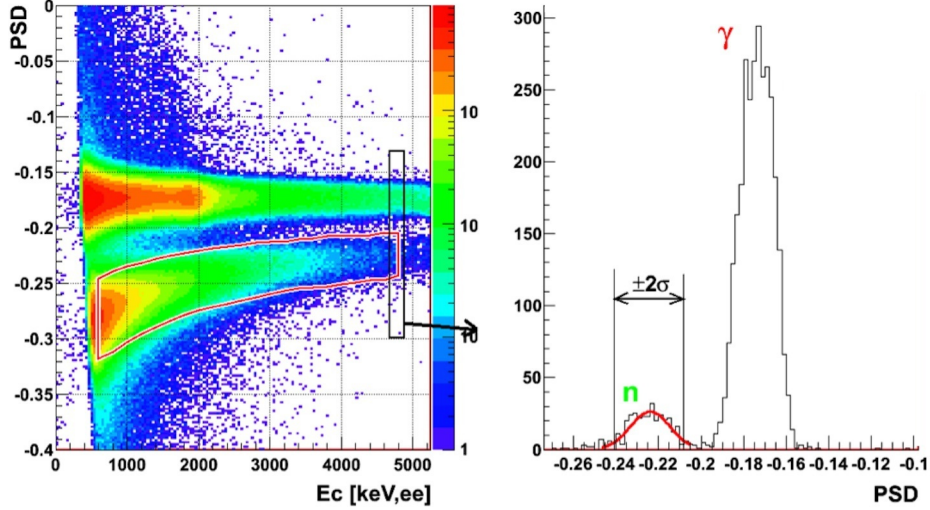


FIG. 4. (Left) pulse shape discrimination (PSD) metric vs. electron equivalent keV. The red box indicates the region of signals identified as neutrons. (Right) separation between neutrons and photons in the region just below 5 MeV.

The errors are calculated using the full covariance matrix for a multinomial distribution [58],

$$\sigma_{Y_{2F}}^2 = \frac{1}{N} \sum_n b_n(1-b_n) \frac{n^2}{4\langle n \rangle^4} (n\langle n \rangle - \langle n^2 \rangle - \langle n \rangle^2)^2 - \frac{1}{N} \sum_{n \neq m} b_n b_m \frac{nm}{4\langle n \rangle^4} (n\langle n \rangle - \langle n^2 \rangle - \langle n \rangle^2) (m\langle n \rangle - \langle n^2 \rangle - \langle n \rangle^2). \quad (4)$$

The Y_{2F} values and errors for each exposure were calculated separately and checked for outliers before combining the exposures to calculate a final value and error for each object. The Y_{2F} measurements are listed in Table 2 and plotted in Fig. 5 along with a set of corrected Y_{2F} values that will be discussed in the next section. We note that the uncorrected values illustrate the time dependence expected from Eq. 2. One can also see from the uncorrected beryllium measurements that a significant non-fission component contributes to the uncorrected Y_{2F} values.

gate (ns)	Be		DU		HEU		diff
	Y_{2F}	error	Y_{2F}	error	Y_{2F}	error	σ
16	1.15E-4	1.70E-6	1.82E-4	4.08E-6	1.98E-4	3.46E-6	
corr	-3.25E-7	2.23E-6	4.33E-5	2.19E-6	5.05E-5	1.98E-6	2.4
64	2.58E-4	2.88E-6	4.60E-4	6.62E-6	4.98E-4	5.63E-6	
corr	-2.85E-6	4.44E-6	1.51E-4	4.16E-6	1.78E-4	3.79E-6	4.8
100	2.83E-4	3.31E-6	5.52E-4	7.35E-6	5.95E-4	6.30E-6	
corr	9.33E-7	5.59E-6	2.15E-4	5.04E-6	2.45E-4	4.55E-6	4.5
200	2.98E-4	4.19E-6	6.44E-4	8.32E-6	6.95E-4	7.24E-6	
corr	-5.42E-6	7.87E-6	2.83E-4	6.20E-6	3.20E-4	5.67E-6	4.4
1000	2.54E-4	8.20E-6	7.31E-4	1.15E-5	7.95E-4	1.07E-5	
corr	-6.65E-5	1.75E-5	3.46E-4	1.00E-5	3.98E-4	9.71E-6	3.7
20000	1.73E-4	3.56E-6	6.87E-4	3.85E-5	8.56E-4	3.85E-5	
corr	-1.53E-4	7.89E-5	3.00E-4	3.80E-5	4.10E-4	3.83E-5	2.0

TABLE 2. The Y_{2F} results from the beryllium, and 3-plate DU and HEU assemblies. The second row for each time gate, labeled “corr” gives the value of Y_{2F} after the cross-talk correction is applied.

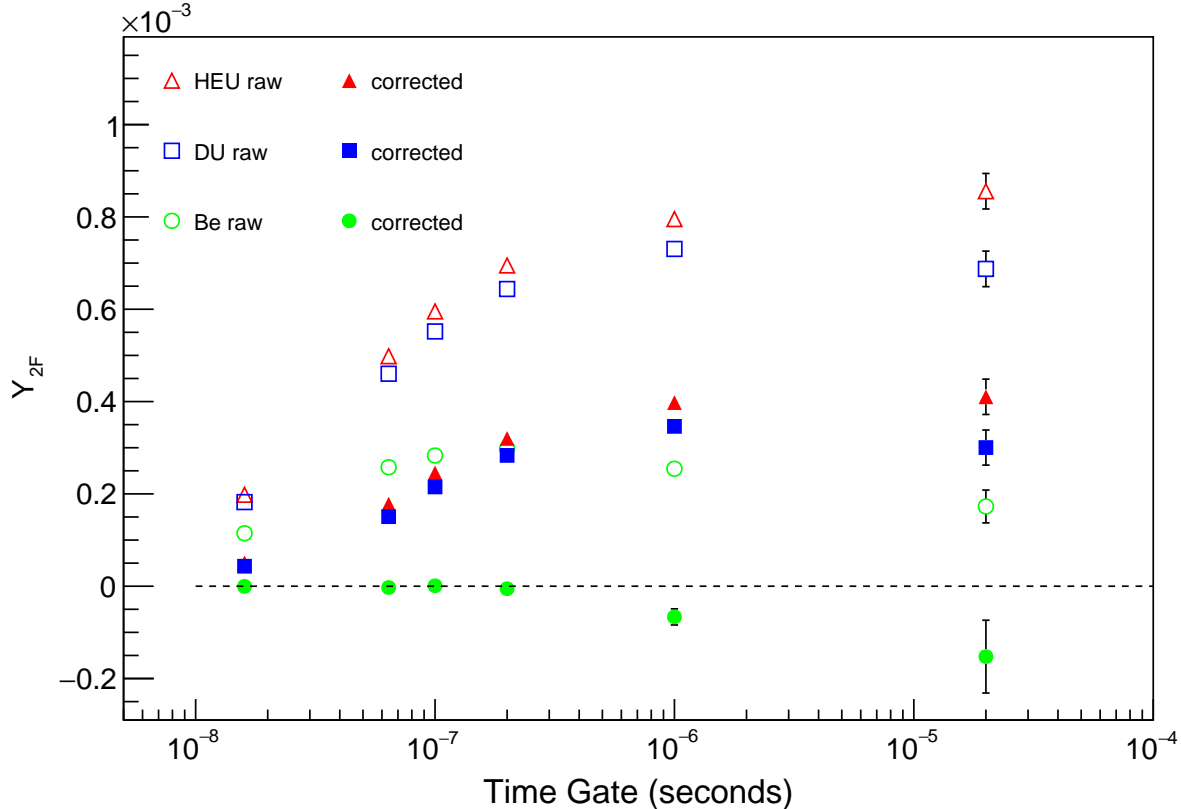


FIG. 5. The time-gate dependence of the measured Y_{2F} signals for the beryllium, DU, and HEU 3-disc stacks. Uncorrected values are plotted as open symbols. The solid symbols show values that have been corrected for cross-talk as explained in Section IV C.

C. Cross-talk Cuts and Corrections

Neutrons that deposit energy in more than one detector will produce a correlated signal that contributes to the Y_{2F} term. This effect is shown clearly in Fig. 6. The left panel shows the distribution of pairs of neutron hits for one DU run as a function of the coincidence time and channel separation for channels in the same array column. Adjacent channels within a single column are separated by a distance of 18.5 cm. For $\Delta\text{chan} = 1$, 90% of these channels are separated by this distance, with the remaining 10% separated by a distance of 2 meters or greater. $\Delta\text{chan} = 2$, 80% are separated by a distance of 37 cm. The corresponding distribution for a GEANT4 [59] simulation is shown on the right. The DAQ trigger logic rejects new signals within 256 ns after a given trigger, leaving zero entries $\Delta\text{chan} = 0$ row of Fig. 6 creating the empty bins in the top row that is obscured from view. A significant cross-talk effect is evident in the vertically adjacent and next-nearest neighbor channels ($\Delta\text{chan} = 1, 2$). These enhancements are also visible in the GEANT4 simulation shown in the right panel. Additional time-dependent structure in the data is attributed to the neutron-correlations, which were not included in this simulation.

We have corrected for this cross-talk effect on adjacent channels by fitting the time-dependence to a linear function at larger times and extrapolating into the cross-talk region, as shown in the left panel of Fig. 7. The fit was performed for time differences greater than 100 ns, and the integral of the fit was used to calculate the expected signal in the absence of cross-talk. A similar analysis was performed for next-nearest channels. The ratio of actual counts to extrapolated counts for adjacent and next-nearest channels is shown in the right panel Fig. 7. Note that for $\Delta\text{ch} = 2$ the correction returns to unity for times that are smaller than the transit time between the next-nearest neighbor channels. Note that this correction was only used for time differences less than 100 ns, and was not used in the regions above where deviations from unity are dominated by statistical fluctuations. A cross-talk correction was also calculated for the horizontal neighbors separated by 2 meters ($\Delta\text{ch} = 8$) and was found to be negligible.

The Y_{2F} values corrected for cross-talk are listed on the second row of each time-gate in Table 2 and plotted

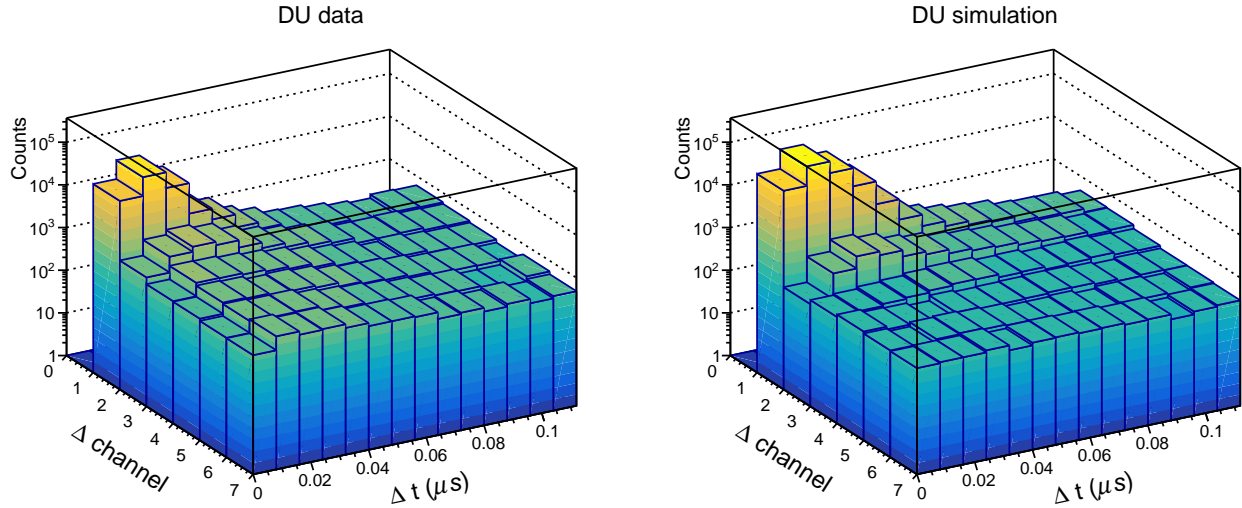


FIG. 6. (Left) distribution of detected neutron pairs over coincidence time and channel difference for one run of DU data and (right) a corresponding GEANT4 simulation. Adjacent channels in the same detector-array column are separated by a distance of 18.5 cm.

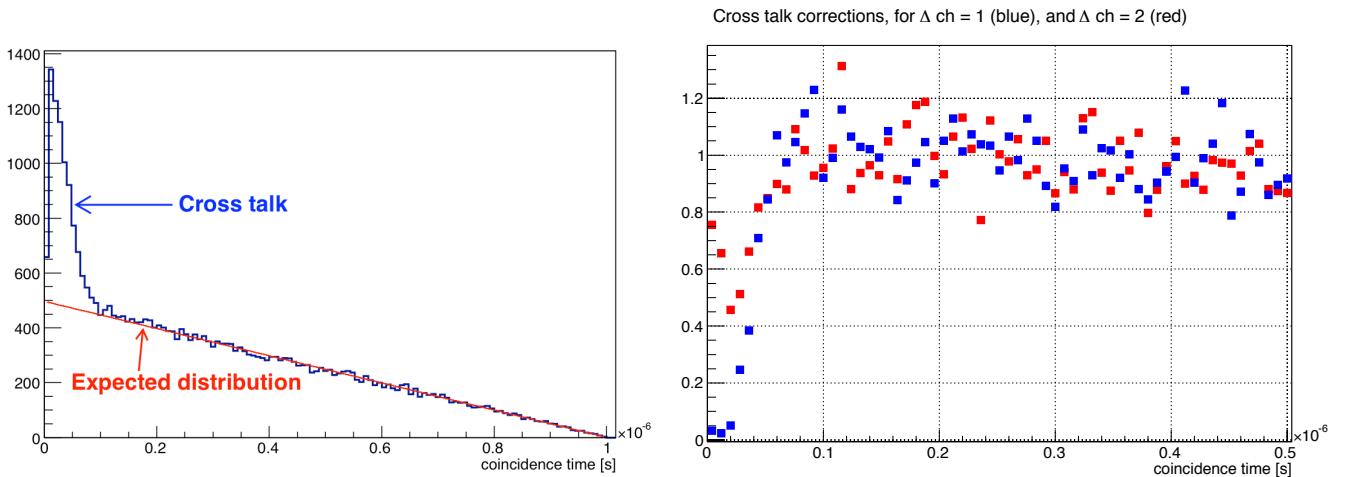


FIG. 7. (Left) the coincidence time distribution for any two pairs of events within a $1 \mu\text{s}$ time gate, for $\Delta ch = 1$. The peak at lower values corresponds to cross-talk between neighboring channels. (Right) cross-talk correction factors for $\Delta ch = 1, 2$.

as solid symbols in Fig. 5. Note that the corrected Y_{2F} values for beryllium are consistent with zero as expected. The difference between Y_{2F} values for the DU and HEU stacked discs, already visible before the application of the correction, is still easily discernible in Fig. 5. Although the Y_{2F} difference grows larger with increasing time-gate, the most significant difference for this measurement, approaching 5-sigma, occurs in the region of 50–100 ns. A time-gate of 100 ns is applied to the analysis of all subsequent measurements.

V. RESULTS AND SIMULATION BENCHMARKS

The Y_{2F} values for 100 ns time-gates and cross-talk corrections for the complete set of objects listed in Table 1 are plotted in Fig. 8 as a function of object multiplication calculated with MCNP. Contrary to expectations based on Eq. 2, the Y_{2F} values do not depend simply on the multiplication. The Y_{2F} values decrease with multiplication for the DU discs, remain approximately constant for the HEU disks, and finally exhibit the expected monotonic

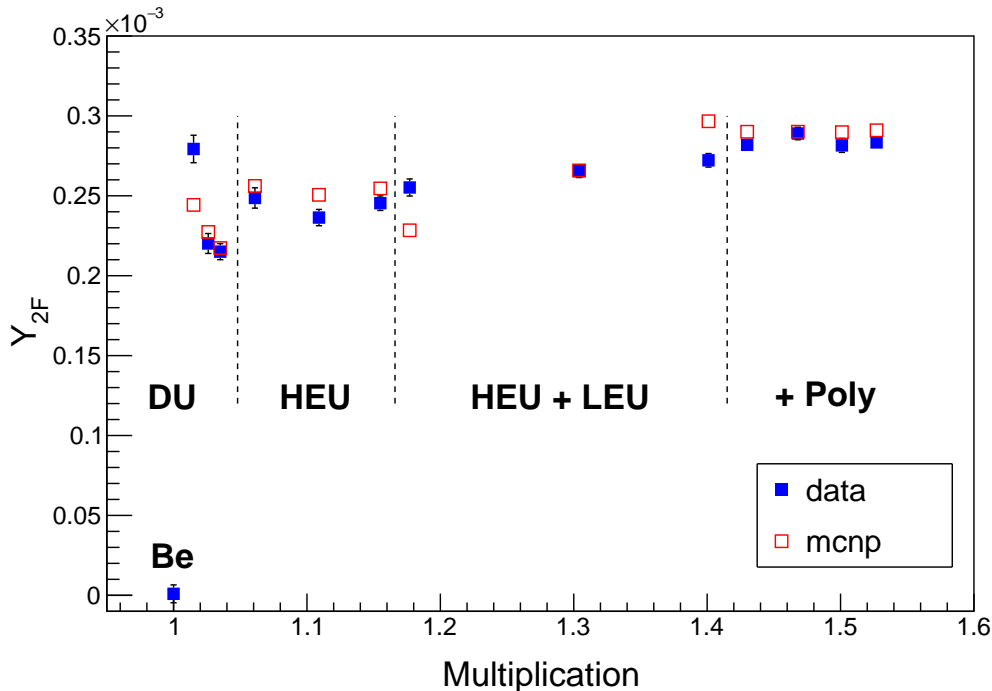


FIG. 8. Measured Y_{2F} for 100 ns time-bins *vs.* Multiplication for all SNM objects measured at the PSI facility in March, 2013. Corresponding MCNP calculations are plotted as open squares.

increase for the composite systems. These results are compared to MCNP simulations of the PSI beam incident on the fissile objects. The detector acceptance was approximated by applying a ± 15 -degree angular cut above and below the horizontal. The angular cut matches the angle subtended by the PNPf detector array, and it is required to account for the polar-angle dependence of the neutron emission rates, which varies with object and is strongest for the LEU+HEU+HDPE composite objects. A minimum energy cut of 1.5 MeV is also applied to the neutrons to approximate the online energy cut implemented in the DAQ. Neutrons within this acceptance region were used to calculate the Y_{2F} in the same manner as the data, using 100 ns time-gates, but without the need for cross-talk corrections. A geometric efficiency factor of 0.25% was applied to the simulated Y_{2F} values. This value was determined empirically and is comparable to the 0.243% geometric detector efficiency calculated in GEANT4. The MCNP results reproduce the overall trends of the data, although the simulations under-predict the decrease for DU and over-predict the increase for the LEU+HEU composite object. The highest multiplication objects consisting of the interleaved LEU and HEU objects with HDPE moderation are reasonably well-reproduced by the MCNP simulations.

This complex dependence of the Y_{2F} values that was observed in the data and qualitatively reproduced by the simulation led us to reconsider some of the assumptions within Eq. 2. One important modification is to account for the fact that in photon-induced fissions, the initial fission differs from those of subsequent neutron-induced fissions in the chain. This is analogous to the modification required for spontaneous fission-chains developed by Prasad and Snyderman [55]. The initial photo-fission is especially important for small multiplication values, where the neutrons from the initial fission form a non-negligible contribution to Y_{2F} . We introduce ν_γ for the mean number of neutrons produced in a photo-fission, and $\nu_{\gamma 2}$ for the half-variance. We also account for the non-fission photo-production and absorption in the extended object by adding the terms f_o for the fraction of neutrons emitted from fission over the total number of neutrons produced by all nuclear reactions and ϵ_o for the neutron absorption within the object. The neutron detection efficiency is denoted separately as ϵ_d . Accounting for these additional factors yields the following expression for Y_{2F} for photon-induced fissions in an extended object,

$$Y_{2F} = f_o \epsilon_o \epsilon_d \left[\frac{\nu_{\gamma 2}}{\nu_\gamma} + \frac{\nu_2}{\nu} (M - 1) \right] \left[1 + \frac{\nu - 1}{\nu} (M - 1) \right] \quad (5)$$

The mean number of neutrons per photon-fission, ν_γ has been measured by Caldwell *et al.* [60] and evaluated by Chadwick [61], however, the value for $\nu_{\gamma 2}$ has not yet been measured. To estimate this value within the simulation, a

Enrichment	$\bar{\nu}$	$\bar{\nu}_2$	$\bar{\nu}_\gamma$	$\bar{\nu}_{\gamma 2}$
DU (0%)	2.43	2.45	2.78	3.09
LEU (20%)	2.45	2.52	2.75	3.04
HEU (93%)	2.51	2.63	2.63	2.90
U-235 (100%)	2.52	2.65	2.62	2.86

TABLE 3. First and second combinatorial moments for photon and neutron induced fission for various levels of uranium enrichment. Neutron induced moments are calculated from Holden and Zucker tables for 1–2 MeV neutrons reported in the documentation for the MCNP fission package. Photon induced moments are calculated from the photo-fission model using the PSI beam energy spectrum.

separate simulation of the MCNP photo-fission package was performed using the PSI energy spectrum as input. The mean and half-variance values for photon-induced fissions obtained in this way are listed in Table 3. We also list the corresponding values for neutron-induced fissions as reported by Zucker and Holden [62]. To compare our simulations to Eq. 5, which does not include energy dependence, we remove all energy cuts from the analysis, and we lengthen the Y_{2F} time-gate for this simulation to 1 ms, to encompass the correlation-time for all neutrons, including thermal. The values for f_o and ϵ_o were taken from the simulations and a perfect detector efficiency ($\epsilon_d = 1$) was assumed. The full comparison between this MCNP simulation and Eq. 5 is shown in Fig. 9. Eq. 5 accounts for the

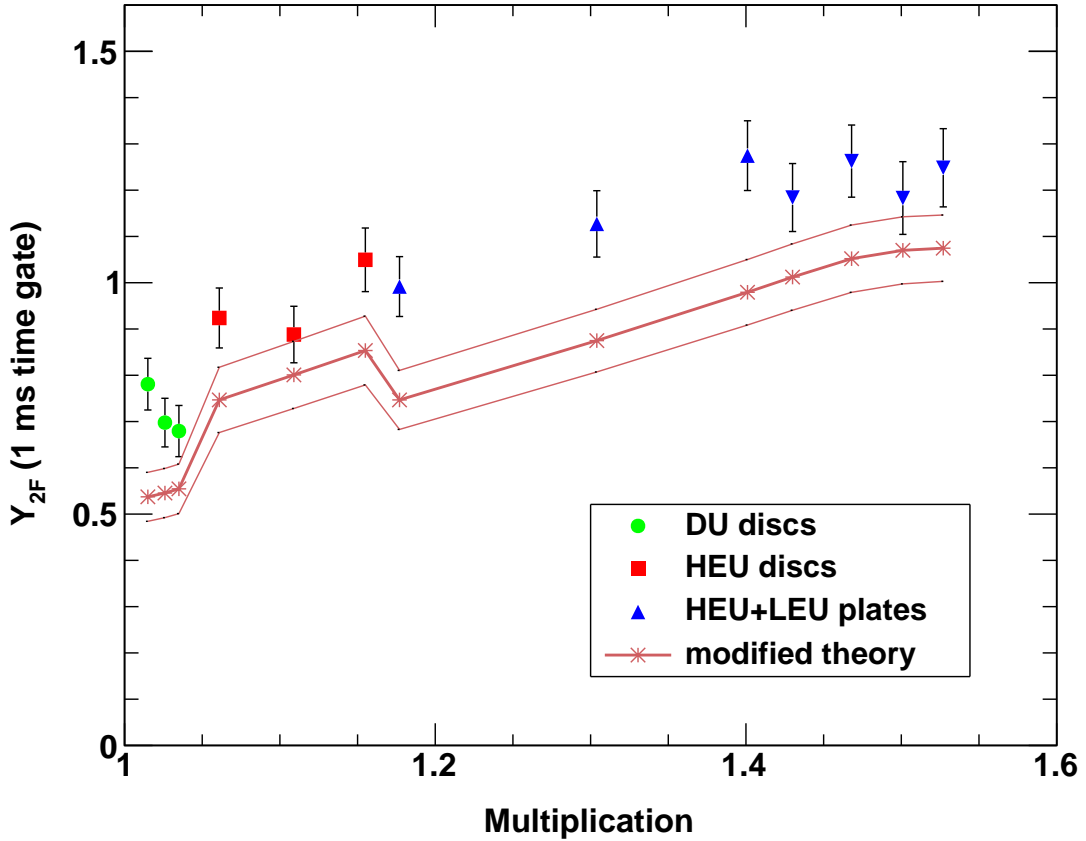


FIG. 9. Comparison of Eq. 5 to MCNP simulations of Y_{2F} vs. Multiplication for all SNM objects measured at the Passport facility. The lines representing Eq. 5 show the impact of a 10% variation in the value of the photo-fission neutron variance, $\nu_{\gamma 2}$, which is currently unmeasured.

full multiplication dependence observed in the simulations, but consistently under-predicts the Y_{2F} values by 20%. One possible explanation for this discrepancy is the lack of energy dependent terms in Eq. 5. It is also possible that our estimate for the unmeasured $\nu_{\gamma 2}$ differs from the value used in the full simulation. The Y_{2F} values can be very sensitive to the value of $\nu_{\gamma 2}$ for objects with low multiplication. To illustrate the sensitivity of Y_{2F} to the value of

Mass (kg)	radius (cm)	M-DU	M-HEU
0.01	0.500	1.016	1.064
0.02	0.630	1.020	1.082
0.05	0.855	1.027	1.115
0.1	1.077	1.033	1.149
0.2	1.357	1.041	1.197
0.5	1.842	1.056	1.289
1	2.321	1.071	1.398
2	2.924	1.088	1.554
5	3.969	1.115	1.941
10	5.000	1.143	2.545
20	6.300	1.173	4.107
50	8.550	1.219	104.1

TABLE 4. Mass, radius, and Multiplication values for DU and HEU spherical objects interrogated with 9-MeV *bremstrahlung* gamma distribution in simulation.

$\nu_{\gamma 2}$, we vary its value by $\pm 10\%$, as shown by the upper and lower bands.

VI. SYSTEM PERFORMANCE PREDICTIONS

With the MCNP simulations benchmarked by experimental results and qualitatively supported by an underlying theory, additional simulations of shorter exposures with larger masses were performed to predict PNP system performance for distinguishing between DU and HEU in shielded configurations. For this study we performed simulations for a set of 24 solid spheres of DU and HEU spanning a range of masses from 10 grams up to 50 kilograms. The masses, radii, and multiplication values are given in Table 4. MCNP simulations were performed for these objects using a PSI beam of 200 μA beam for a 10 second exposure. The emitted neutrons were collected over the entire acceptance and multiplied by the overall geometric efficiency factor of 0.25% to match the experiment. A lower minimum energy cut of $E > 1 \text{ MeV}$ was used, based upon potential improvements to the neutron identification, and a nominal time-gate of 100 ns was used for calculated Y_{2F} values.

Although the Y_{2F} values are calculated directly from the simulations, we chose to use experimental data to extrapolate errors. Fig. 10 shows a uniform, linear dependence in the Y_{2F} error as a function of $N_{\text{counts}}^{-1/2}$, independent of object type. The data are well fit to the following functional form,

$$\sigma_{Y_{2F}}(N_{\text{counts}}) = 2.43 \times 10^{-6} + \frac{0.011}{\sqrt{N_{\text{counts}}}}. \quad (6)$$

We note that this formula does not extrapolate to zero error for zero counts, consistent with the fact that the errors are not strictly Poisson-distributed. This scaling is used to rescale our simulations for different objects and shielding configurations to predict the dependence on exposure time.

Using the simulated Y_{2F} values and errors extrapolated from data, we use a Gaussian classifier to establish Receiver Operating Characteristics (ROC) curves for the purpose of distinguishing between HEU and DU objects. Using the HEU as the alarm scenario and the DU as the null scenario we can assign as “positive” value based on a Gaussian probability threshold:

$$\mathcal{P} = 1 - \int_T^{\infty} dY_{2F} \frac{1}{\sqrt{2\pi}\sigma} e^{-(Y^{exp} - Y_{2F})^2 / 2\sigma^2} \quad (7)$$

where Y^{exp} is the measured Y_{2F} and σ is the extrapolated error.

The ROC curves for different unshielded object masses are shown in Fig. 11 for spherical objects of 2, 5, 10, and 20 kg. For every object the ROC values were determined for the current PSI detector configuration (solid lines) and for one with $4\times$ increased geometric efficiency. The analysis shows that while detection of small objects, e.g. 2kg, may be difficult, for larger objects the signal becomes large enough for a fast detection. This becomes especially true for a larger detector array. Note that the positive detection of 20 kg sphere with the $4\times$ augmented detector array approaches 100% with a very low rate for false positives.

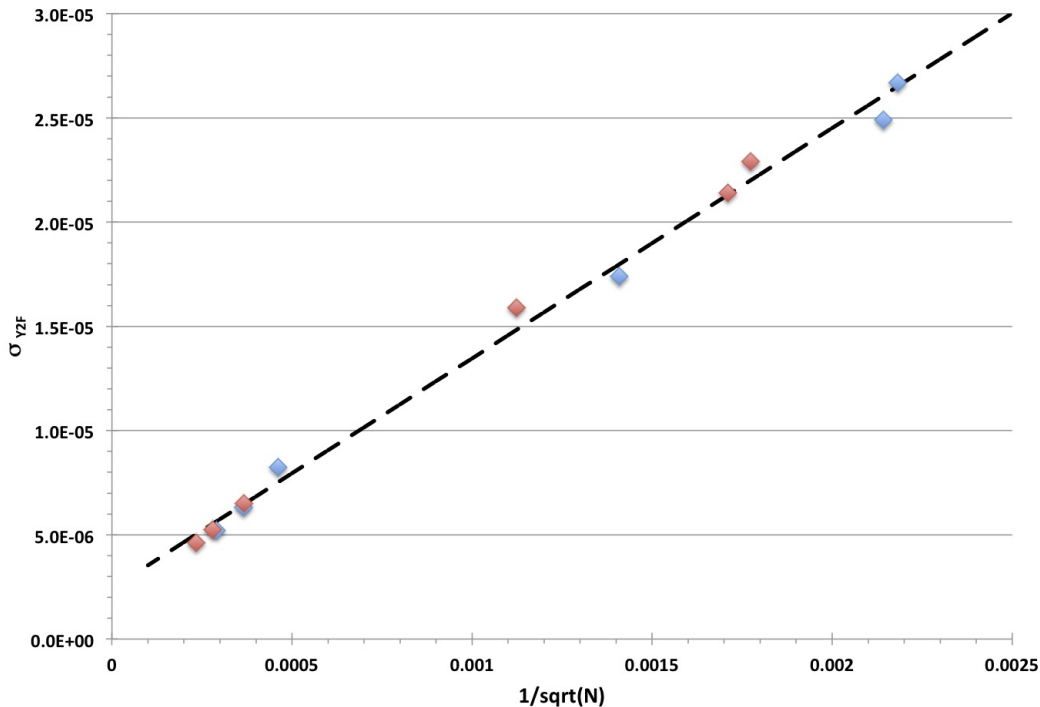


FIG. 10. Data for the 300s and full duration runs. Red diamonds are the HEU points, blue diamonds the DU points. The uncertainty scales with the inverse square root of the total counts.

In addition to characterizing performance for unshielded objects, the system was also studied for shielded configurations, where the 5 kg objects were surrounded by iron and HDPE blocks of varying thickness. The first shielding scenario has the primary effect of reducing the incident photon flux, thus reducing statistics in a fixed measurement time. The second scenario's impact primarily consists of moderating the fast neutrons, and thus reduces neutron statistics. Figures 12 shows the ROC curves for the 5 kg object for several thickness of full density iron (left) and HDPE shielding (right).

VII. CONCLUSIONS

The objective of the experimental effort described in this work was to extend the already existing Prompt Neutrons from Photofission (PNPF) technique, described in Ref. [35], to distinguish between fissionable (e.g. DU) and fissile (e.g. HEU, WGPu) materials by using neutron multiplicity analysis. The goal of the initial stages of the experimental program was to develop the necessary statistical and mathematical formalism, the Monte Carlo simulation infrastructure, and to experimentally demonstrate the feasibility of the technique. The results showed a 5-sigma difference in the signal for the two types of objects, proving the feasibility of this methodology.

The next stages of the program focused on additional experiments, involving more complex target configurations using DU, LEU, and HEU. The Y_{2F} measurements were compared to simulations, which in turn were used to develop a theoretical-numerical model providing a basis for extrapolations to larger objects and shorter exposure times. The results showed that while the Y_{2F} signal is marginal for practical differentiation of the small objects used in the experiment, for 5kg spherical sizes the neutron multiplication M is large enough to differentiate fissile material types in shielded cargo configurations with reasonable scan times.

While both the feasibility and practicality of the methodology was demonstrated, significant additional work remains to be done. Measurements on a wider range of object sizes, both large and small, would be valuable for further understanding the dynamics of Y_{2F} . Also high statistics measurement of photo-fission neutron distributions with thin-foil U-235 and U-238 targets with large acceptance detector that would enable precise and accurate determination of $\nu_{\gamma 2}$ would significantly reduce uncertainties for future system performance studies.

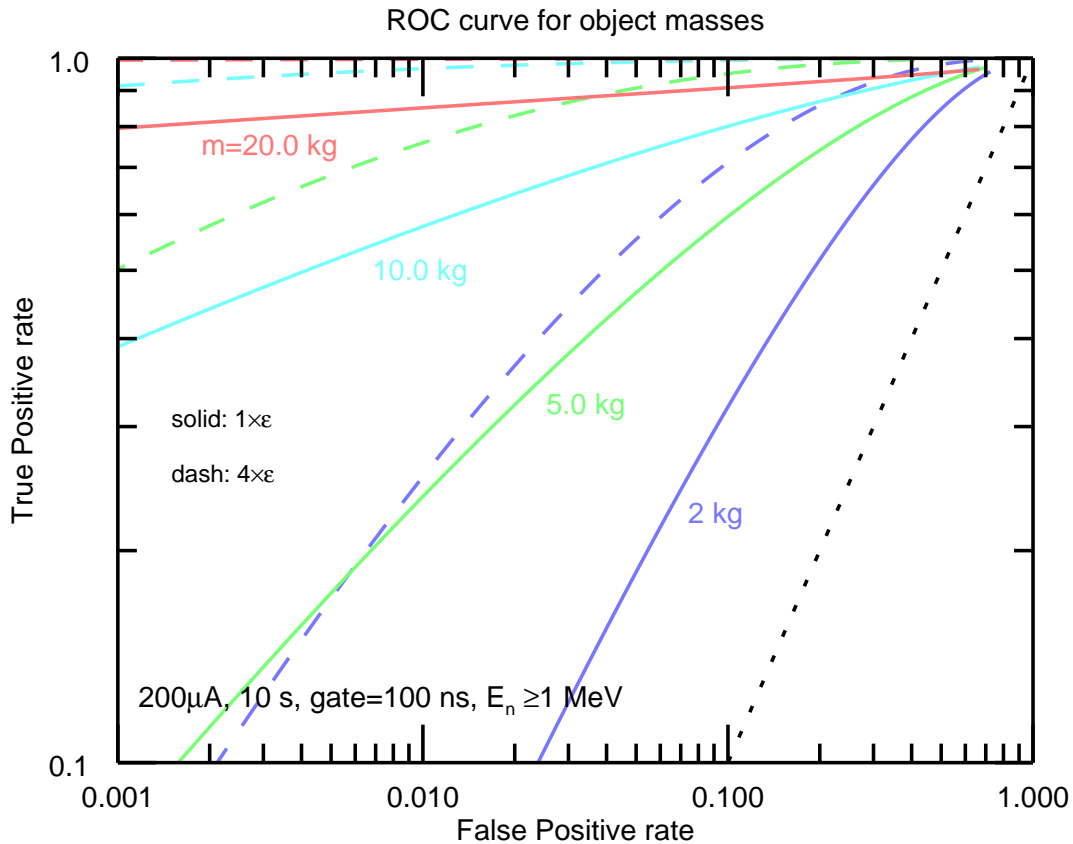


FIG. 11. ROC curves for distinguishing HEU from DU in 10 seconds of 200 μ A beam for 2, 5, 10, and 20 kg spherical objects. Solid lines are for the existing Passport system efficiency, dashed lines show the improvement for a 4 \times increase in efficiency. The curve for 20kg object at 4 \times efficiency is consistent with True Positive Rate = 1.

VIII. ACKNOWLEDGEMENTS

The authors wish to acknowledge helpful conversations with Dr. George Chapline and Prof. William Bertozzi. The authors thank Cody Wilson of PSI for his help in running the accelerator and the system. This work is supported in part by the U.S. Department of Homeland Security Domestic Nuclear Detection Office through a collaboration between Lawrence Livermore National Laboratory and Passport Systems, Inc. Lawrence Livermore National Laboratory is operated by Lawrence Livermore National Security, LLC, for the U.S. Department of Energy, National Nuclear Security Administration under Contract DE-AC52-07NA27344.

REFERENCES

-
- [1] P. Campbell, E. M. Gardy, and D. G. Boase, *Assay of Fissionable Isotopes in Aqueous Solution by Pulsed Neutron Interrogation*, Tech. Rep. AECL-5994 (Atomic Energy of Canada Limited, 1978).

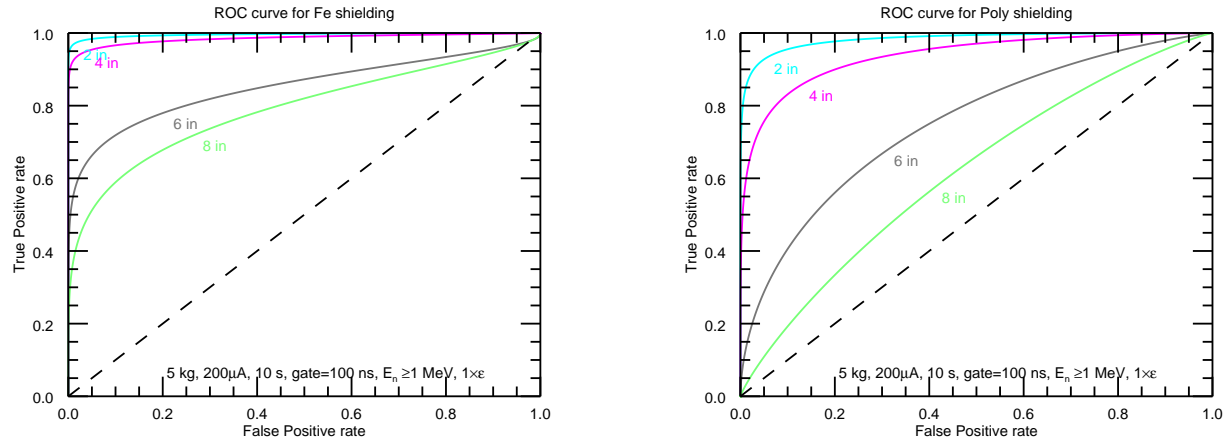


FIG. 12. ROC curves for distinguishing HEU from DU with 10 s of 200 μ A beam for 5 kg objects with 2, 4, 6, 8 inches shielding of Fe (left) and HDPE (right) spherical shells surrounding the objects.

- [2] C. L. Hollas, C. A. Goulding, and W. L. Myers, *Nondestructive analysis of shielded highly enriched uranium*, Tech. Rep. LA-UR-01-1881 (Los Alamos National Laboratory, 2001).
- [3] D. Slaughter, M. Accatino, A. Bernstein, J. Candy, A. Dougan, J. Hall, A. Loshak, D. Manatt, A. Meyer, B. Pohl, S. Prussin, R. Walling, and D. Weirup, *Detection of special nuclear material in cargo containers using neutron interrogation*, Tech. Rep. UCRL-ID-155315 (Lawrence Livermore National Laboratory, 2003).
- [4] X. Lia, R. Henkelmann, and F. Baumgärtner, *Nucl. Instrum. Meth. B* **215**, 246 (2004).
- [5] D. Dietrich, C. Hagmann, P. Kerr, L. Nakae, M. Rowland, N. Snyderman, W. Stoeffl, and R. Hamm, *Nucl. Instrum. Meth. B* **241**, 826 (2005).
- [6] J. L. Jones, W. Y. Yoon, Y. D. Harker, J. M. Hoggan, K. J. Haskell, and L. A. VanAusdeln, *Proof-of-Concept Assessment of a Photofission-Based Interrogation System for the Detection of Shielded Nuclear Material*, Tech. Rep. INEEL/EXT-2000-01523 (Idaho National Engineering and Environmental Laboratory, 2000).
- [7] J. L. Jones, K. J. Haskell, J. M. Hoggan, and D. R. Norman, *ARACOR Eagle- Matched Operations and Neutron Detector Performance Tests*, Tech. Rep. INEEL/EXT-02-00823 (Idaho National Engineering and Environmental Laboratory, 2002).
- [8] J. L. Jones, W. Y. Yoon, K. J. Haskell, D. R. Norman, J. M. Hoggan, C. E. Moss, C. A. Goulding, C. L. Hollas, W. L. Myers, and E. Franco, *Photofission-based, Nuclear Material Detection: Technology Demonstration*, Tech. Rep. INEEL/EXT-02-01406 (Idaho National Engineering and Environmental Laboratory, 2002).
- [9] J. L. Jones, K. J. Haskell, J. M. Hoggan, D. R. Norman, and W. Y. Yoon, *AIP Conf. Proc.* **680**, 947 (2003).
- [10] J. L. Jones, W. Y. Yoon, K. J. Haskell, D. R. Norman, J. M. Zabriskie, J. W. Sterbentz, S. M. Watson, J. T. Johnson, B. D. Bennett, R. W. Watson, and K. L. Folkman, *Pulsed Photonuclear Assessment (PPA) Technique: CY 04 Year-end Progress Report*, Tech. Rep. INEEL/EXT-05-02583 (Idaho National Engineering and Environmental Laboratory, 2005).
- [11] J. L. Jones, B. D. Bennett, K. J. Haskell, J. T. Johnson, D. R. Norman, J. W. Sterbentz, R. W. Watson, S. M. Watson, W. Y. Yoon, J. M. Zabriskie, C. E. Moss, K. L. Folkman, C. C. O'Neil, A. W. Hunt, and R. J. Spaulding, *Pulsed Photonuclear Assessment (PPA) Technique: CY-05 Project Summary Report*, Tech. Rep. INL/EXT-05-01020 (Idaho National Laboratory, 2005).
- [12] J. L. Jones, D. R. Norman, K. J. Haskell, J. W. Sterbentz, W. Y. Yoon, S. M. Watson, J. T. Johnson, J. M. Zabriskie, B. D. Bennett, R. W. Watson, C. E. Moss, and J. F. Harmon, *Nucl. Instrum. Meth. A* **562**, 1085 (2006).
- [13] C. E. Moss, C. L. Hollas, and W. L. Myers, *Active Interrogation of Highly Enriched Uranium*, Tech. Rep. LA-UR-04-3913 (Los Alamos National Laboratory, 2004).
- [14] W. L. Myers, C. A. Goulding, C. L. Hollas, and C. E. Moss, in *Proceedings of the International Conference on Nuclear Data For Science and Technology, September 26 - October 1, Santa Fe, New Mexico, USA* (2004).
- [15] W. L. Myers, C. A. Goulding, C. L. Hollas, and C. E. Moss, *AIP Conf. Proc.* **769**, 1688 (2005).
- [16] J. L. Jones, W. Y. Yoon, D. R. Norman, K. J. Haskell, J. M. Zabriskie, S. M. Watson, and J. W. Sterbentz, *Nucl. Instrum. Meth. B* **241**, 770 (2005).
- [17] J. L. Jones, B. W. Blackburn, D. R. Norman, S. M. Watson, K. J. Haskell, J. T. Johnson, A. W. Hunt, J. F. Harmon, and C. E. Moss, *Nucl. Instrum. Meth. A* **579**, 353 (2007).
- [18] R. C. Runkle, D. L. Chichester, and S. J. Thompson, *Nuclear Instruments and Methods in Physics Research Section A: Accelerators, Spectrometers, Detectors and Associated Equipment* **663**, 75 (2012).
- [19] C. E. Moss, C. A. Goulding, C. L. Hollas, and W. L. Myers, *AIP Conf. Proc.* **680**, 900 (2003).

- [20] D. L. Chichester, S. A. Pozzi, J. L. Dolan, M. T. Kinlaw, A. C. Kaplan, M. Flaska, A. Enqvist, J. T. Johnson, and S. M. Watson, *MPACT Fast Neutron Multiplicity System Design Concepts*, Tech. Rep. INL/EXT-12-27619 (Idaho National Laboratory, 2012).
- [21] M. O. Deighton, Nucl. Instrum. Meth. **165**, 589 (1979).
- [22] G. J. Arnone and G. S. Brunson, *A programmable multichannel correlation module for analyzing neutron multiplicities*, Tech. Rep. LA-UR-89-3538 (Los Alamos National Laboratory, 1989).
- [23] C. L. Hollas, C. A. Goulding, and W. L. Myers, Nucl. Instrum. Meth. A **453**, 559 (2005).
- [24] L. F. Nakae, P. L. Kerr, R. J. Newby, M. K. Prasad, M. S. Rowland, N. J. Snyderman, J. M. Verbeke, and R. E. Wurtz, in *Proceedings of the 2nd Japan IAEA Workshop on Advanced Safeguards Technology for the Future Nuclear Fuel Cycle Tokai, Japan November 10 through November 13* (2009).
- [25] S. McConchie, P. Hausladen, J. Mihalcz, B. Blackburn, and D. Chichester, AIP Conf. Proc. **1099**, 643 (2009).
- [26] K. V. Nixon, E. J. Dowdy, S. W. France, and A. A. Robba, in *Proceedings of the 1982 IEEE Nuclear Science Symposium, Washington, D. C. October 20-22* (1982).
- [27] M. S. Krick and J. E. Swansen, Nucl. Instrum. Meth. **219**, 384 (1984).
- [28] D. M. Cifarelli and W. Hage, Nucl. Instrum. Meth. A **251**, 550 (1985).
- [29] N. Dytlewski, M. S. Krick, and N. Ensslin, Nucl. Instrum. Meth. A **327**, 469 (1993).
- [30] S. M. McConchie, P. Hausladen, and J. T. Mihalcz, “Passive time coincidence measurements with assemblies of HEU and DU castings,” <http://info.ornl.gov/sites/publications/files/Pub20249.pdf> (2009).
- [31] S. M. McConchie, P. Hausladen, and J. T. Mihalcz, in *Proceedings of the 50th Annual Meeting of the Institute for Nuclear Materials Management, Tucson, Arizona* (2009).
- [32] K. E. Peña, S. M. McConchie, and J. T. Mihalcz, in *Proceedings of the INMM 51st Annual Meeting, Baltimore, MD, USA, July 11-15* (2010).
- [33] A. Danagoulian, W. Bertozzi, C. L. Hicks Jr, A. V. Klimenko, S. E. Korbly, R. J. Ledoux, and C. M. Wilson, in *Technologies for Homeland Security (HST), 2010 IEEE International Conference on* (IEEE, 2010) pp. 379–384.
- [34] W. Bertozzi and R. Ledoux, “Non-intrusive method to identify presence of nuclear materials using energetic prompt neutrons from photon-induced fission,” (2014), uS Patent 8,718,219.
- [35] A. Danagoulian *et al.*, in *Technologies for Homeland Security (HST), 2010 IEEE International Conference on* (IEEE, 2010) pp. 379–384.
- [36] R. P. Feynman, F. D. Hoffmann, and R. Serber, J. Nucl. Energy (1954) **3**, 64 (1956).
- [37] S. B. Degweker, Ann. Nucl. Energy **24**, 1 (1997).
- [38] S. B. Degweker, Ann. Nucl. Energy **24**, 375 (1997).
- [39] S. B. Degweker, Ann. Nucl. Energy **24**, 1301 (1997).
- [40] S. B. Degweker, Ann. Nucl. Energy **26**, 387 (1999).
- [41] S. B. Degweker, Ann. Nucl. Energy **27**, 1245 (2000).
- [42] J. L. Muñoz-Cobo and G. Verdú, Ann. Nucl. Energy **14**, 327 (1987).
- [43] J. L. Muñoz-Cobo, R. B. Perez, and G. Verdú, Nucl. Sci. Eng. **95**, 83 (1987).
- [44] S. B. Degweker, Ann. Nucl. Energy **21**, 531 (1994).
- [45] S. B. Degweker, Ann. Nucl. Energy **30**, 223 (2003).
- [46] D. Ballester and J. L. Muñoz-Cobo, Ann. Nucl. Energy **32**, 493 (2005).
- [47] D. Ballester, J. L. Muñoz-Cobo, and J. L. Kloosterman, Ann. Nucl. Energy **32**, 1476 (2005).
- [48] D. Ballester and J. L. Muñoz-Cobo, “The pulsing CPSD method for subcritical assemblies with pulsed sources,” (2005), arXiv:physics/0506166.
- [49] A. A. Robba, E. J. Dowdy, and H. F. Atwater, Nucl. Instrum. Meth. **215**, 473 (1983).
- [50] E. J. Dowdy, G. E. Hansen, and A. A. Robba, *Feynmann variance-to-mean method*, Tech. Rep. LA-UR-85-3073 (Los Alamos National Laboratory, 1985).
- [51] G. P. Estes and C. A. Goulding, *Subcritical multiplication determination studies*, Tech. Rep. LA-UR-95-2016 (Los Alamos National Laboratory, 1995).
- [52] S. Croft, A. Favalli, D. K. Hauck, D. Henzlova, and P. A. Santi, Nucl. Instrum. Meth. A **686**, 136 (2012).
- [53] C. L. Hollas, C. A. Goulding, and W. L. Myers, *Subcritical Neutron Multiplication Measurements of HEU Using Delayed Neutrons as the Driving Source*, Tech. Rep. LA-UR-99-2192 (Los Alamos National Laboratory, 1999).
- [54] N. Snyderman and M. Prasad, *Appendix A: Theory of Fission Chains and Count Distributions*, Tech. Rep. UCRL-TR-218042 (Lawrence Livermore National Laboratory, 2005).
- [55] M. K. Prasad and N. J. Snyderman, Nucl. Sci. and Eng. **172**, 300 (2012).
- [56] S. Walston, *The Idiot’s Guide to the Statistical Theory of Fission Chains*, Tech. Rep. LLNL-TR-414245 (Lawrence Livermore National Laboratory, 2011).
- [57] t. . C.J. Werner, *et al.*, Tech. Rep.
- [58] P. D. Barnes, Jr., *Calculating the Errors on the Feynman Variance, Y2F*, Tech. Rep. LLNL-TR-414706 (Lawrence Livermore National Laboratory, 2009).
- [59] S. Agostinelli *et al.*, Nuclear Instruments and Methods in Physics Research Section A: Accelerators, Spectrometers, Detectors and Associated Equipment **506**, 250 (2003).
- [60] J. T. Caldwell, E. J. Dowdy, R. A. Alvarez, B. L. Berman, and P. Meyer, Ann. Nucl. Sci. Eng. **73**, 153 (1980).
- [61] *et al.* M. B. Chadwick, Nucl. Instr. Meth. **107**, 2391 (2006).
- [62] M. S. Zucker and N. E. Holden, *Energy Dependence of Neutron Multiplicity in Fast-Neutron-Induced Fission for 235,238U and 239P*, Tech. Rep. BNL-38491 (Brookhaven National Laboratory, 1986).